

Lead-free hybrid organic-inorganic perovskites for solar cell applications

Cite as: J. Chem. Phys. **152**, 014104 (2020); <https://doi.org/10.1063/1.5128603>

Submitted: 20 September 2019 . Accepted: 12 December 2019 . Published Online: 03 January 2020

Vu Ngoc Tuoc , and Tran Doan Huan 



View Online



Export Citation



CrossMark

ARTICLES YOU MAY BE INTERESTED IN

[Capturing static and dynamic correlation with \$\Delta\$ NO-MP2 and \$\Delta\$ NO-CCSD](#)

The Journal of Chemical Physics **152**, 014101 (2020); <https://doi.org/10.1063/1.5140669>

[Green's function coupled cluster simulation of the near-valence ionizations of DNA-fragments](#)

The Journal of Chemical Physics **152**, 011101 (2020); <https://doi.org/10.1063/1.5138658>

[Crystal structures and rotational dynamics of a two-dimensional metal halide perovskite \(OA\)₂PbI₄](#)

The Journal of Chemical Physics **152**, 014703 (2020); <https://doi.org/10.1063/1.5131667>





Lock-in Amplifiers



Zurich
Instruments

Watch the Video



Lead-free hybrid organic-inorganic perovskites for solar cell applications

Cite as: J. Chem. Phys. 152, 014104 (2020); doi: 10.1063/1.5128603

Submitted: 20 September 2019 • Accepted: 12 December 2019 •

Published Online: 3 January 2020



Vu Ngoc Tuoc^{1,a)}  and Tran Doan Huan^{2,b)} 

AFFILIATIONS

¹Institute of Engineering Physics, Hanoi University of Science and Technology, 1 Dai Co Viet Road, Hanoi, Vietnam

²School of Materials Science and Engineering, Georgia Institute of Technology, 771 Ferst Drive NW, Atlanta, Georgia 30332, USA

^{a)}Electronic mail: tuoc.vungoc@hust.edu.vn

^{b)}Electronic mail: huan.tran@mse.gatech.edu

ABSTRACT

Within materials informatics, a rapidly developing subfield of materials research, past (curated) data are mined and learned for either discovering new materials or identifying new functionalities of known materials. This paper provides an example of this process. Starting from a recently developed (very diverse) dataset which includes 1346 hybrid organic-inorganic perovskites (HOIPs), we downselect a subset of 350 three dimensional HOIPs to a final set of four lead-free HOIPs, including $\text{CH}_3\text{NH}_3\text{SnI}_3$, $\text{HC}(\text{NH}_2)_2\text{SnI}_3$, $\text{NH}_2\text{NH}_3\text{SnI}_3$, and $\text{NH}_2(\text{CH}_2)_3\text{SnI}_3$, in which the first two were experimentally synthesized and the others remain hypothetical. Using first-principles based computational methods, we show that these HOIPs have preferable electronic band structures and carrier effective mass, good optical properties, and high spectroscopic limited maximum efficiency. Compared to the experimental data, we find that *state-of-the-art* numerical methods can predict the electronic and optical properties fairly well, while the current model for the spectroscopic limited maximum efficiency is inadequate for capturing the power conversion efficiency of a solar absorber. We suggest that the HOIP dataset should be expanded to include larger structures of HOIPs, thereby being more useful for future data-mining and machine-learning approaches.

Published under license by AIP Publishing. <https://doi.org/10.1063/1.5128603>

I. INTRODUCTION

Data are probably the most essential infrastructure of materials informatics, the subfield of materials research that has been picking up enormous momentum during the last several years.^{1–4} Most of the data accumulated in (and supplied by) the current major materials databases such as Materials Project,⁵ Open Quantum Materials Databases,⁶ NoMAD, PolyInfo, and Polymer Genome³ were generated by first-principles computations, e.g., using density functional theory (DFT).^{7,8} First, this current preference is based on the fairly high fidelity of DFT in computing some (of course, not all) useful properties of solid materials, e.g., electronic structures. Second, powerful computing infrastructures and efficient DFT packages allow computed materials data to be generated in a high-throughput, controllable, and consistent manner. Data prepared in this way^{9–12} are suitable for the modern data-mining and machine-learning methods

to be used efficiently.^{3,4} From the other side, materials data generated via experimental measurements, which are expected to emerge rapidly in the next several years when high-throughput measurements and/or text mining approaches, e.g., natural language processing, become reliable, will also be critical for materials informatics.

This paper showcases a practical application of a computational dataset of hybrid organic-inorganic perovskites (HOIPs)¹⁰ in exploring the chemical space and identifying promising candidates for a given application. HOIPs belong to a class of crystalline materials, which resemble the prototype structures of perovskites (ABX_3) while replacing the inorganic cation A by an organic cation such as CH_3NH_3 (or methylammonium) and $\text{HC}(\text{NH}_2)_2$ (or formamidinium). When $\text{B} = \text{Pb}$ and $\text{X} = \text{I}$, the resulted HOIPs, i.e., $\text{CH}_3\text{NH}_3\text{PbI}_3$ and $\text{HC}(\text{NH}_2)_2\text{PbI}_3$, are very promising candidates for solar cell applications, featuring a power conversion efficiency (PCE) up to 22%.^{13–15} However, these lead-containing materials are

toxic and rapidly degrade when being exposed to light, temperature, oxygen, and moisture.^{14,15} Despite enormous efforts during the last 10 years, they remain the primary obstacles to transforming $\text{CH}_3\text{NH}_3\text{PbI}_3$ and $\text{HC}(\text{NH}_2)_2\text{PbI}_3$ into real-life applications.^{16,17} In particular, replacing Pb by Sn in these HOIPs makes them safe, but their PCE is reduced to $\sim 7\%$ or below.¹⁷ For the degradation problem, it was claimed^{15,18–20} that partially or completely substituting methylammonium CH_3NH_3 with other cations, e.g., a mixture of cesium and $\text{HC}(\text{NH}_2)_2$, could improve the thermal and light stability. This finding is intriguing, suggesting that an exploration over the possible organic cation A, group 14 elements B, and halogens X can deepen our understanding of the HOIP stability and may bring us closer to a solution for this challenging problem. Within this context, some available datasets of HOIPs^{10,21} are particularly useful. One of them, which was developed by us,¹⁰ features 16 possible inorganic cations A, 3 cations B (Pb, Sn, and Ge), 4 halides (I, Br, Cl, and F), and a variety of structural motifs that in turn determine the bandgap E_g ,²² the most important property of solar energy materials.

In this paper, the HOIP dataset¹⁰ is explored for identifying some candidates that can be promising for solar cell applications. From 1346 hybrid organic-inorganic perovskites of the dataset,¹⁰ methylammonium tin iodide $\text{CH}_3\text{NH}_3\text{SnI}_3$, formamidinium tin iodide $\text{HC}(\text{NH}_2)_2\text{SnI}_3$, hydrazinium tin iodide $\text{NH}_2\text{NH}_3\text{SnI}_3$, and azetidinium tin iodide $\text{NH}_2(\text{CH}_2)_3\text{SnI}_3$ were identified for more in-depth studies. Our DFT calculations, which focus on the electronic structure (bandgap and carrier effective masses), optical properties (dielectric functions and absorption coefficient), and spectroscopic limited maximum efficiency (SLME), show that these materials have preferable electronic, optical, and absorption characteristics for being used as solar absorbers. Except for SLME (which was significantly overestimated), the other computed properties agree well with the experimental data of $\text{CH}_3\text{NH}_3\text{SnI}_3$ ^{23–25} and $\text{HC}(\text{NH}_2)_2\text{SnI}_3$.²⁵ No experimental report for $\text{NH}_2\text{NH}_3\text{SnI}_3$ and $\text{NH}_2(\text{CH}_2)_3\text{SnI}_3$ is available as these materials remain hypothetical.

Putting our computational predictions in the context of the experimental realizations of $\text{CH}_3\text{NH}_3\text{SnI}_3$ ^{23–25} and $\text{HC}(\text{NH}_2)_2\text{SnI}_3$,²⁵ we find that *state-of-the-art* DFT-based numerical methods are good in predicting the electronic structures and optical properties of HOIPs but not the spectroscopic limited maximum efficiency, for which more sophisticated models are needed. Moreover, data-driven approaches are promising, but a bigger and better dataset of HOIPs is needed. In particular, larger-cell HOIPs, e.g., the tetragonal and orthorhombic phases, should be included, and numerous organic cations A, which were experimentally realized, should also be considered for expanding HOIP databases, thereby being more useful in exploring the chemical space of this materials class. For $\text{NH}_2\text{NH}_3\text{SnI}_3$ and $\text{NH}_2(\text{CH}_2)_3\text{SnI}_3$, we believe that if being synthesized, they may be similar to or slightly better than $\text{CH}_3\text{NH}_3\text{SnI}_3$ in terms of the properties needed for solar cell applications.

II. METHODS

The dataset of 1346 HOIPs¹⁰ supplies the DFT optimized low-energy structures and other useful properties, including the (fundamental) bandgap E_g computed using generalized gradient approximation (GGA)^{26,27} and Heyd-Scuseria-Ernzerhof

(HSE06)^{28,29} functionals for the exchange-correlation (XC) energies. Because the HOIP structures were predicted using the (very expensive) minima-hopping structure prediction method^{30,31} without constraints, the dataset is limited in terms of the structure size (1 formula unit per cell) but enormously diverse in terms of not only chemistry but also structural (geometrical) motifs.^{32–35} In about 350 entries, the BX_6 octahedra are linked by sharing their corners, distributing throughout three dimensions (3D) of the space, while in the remaining entries, the BX_6 octahedra share their edges and are arranged in one (1D) or two (2D) dimensional substructures (motifs). The structure diversity translates into the diversity in materials properties. Specifically, the bandgap of 3D HOIPs is $E_g \approx 1\text{--}2\text{ eV}$, while for 1D and 2D HOIPs, $E_g \gtrsim 2\text{--}3\text{ eV}$ and above.^{10,22} For solar cell applications, 1D and 2D HOIPs are generally considered photoinactive, and only the 3D HOIPs are suitable. Therefore, 20 lead-free candidates whose (computed) HSE06 bandgap is below 1.8 eV were selected from the subset of 350 3D HOIPs for high-density k -point GGA electronic band structure calculations. A pool of 4 candidates with smallest electron effective mass were finally selected for an expensive in-depth DFT study.

Our first-principles calculations were performed at the level of DFT using the projector augmented wave (PAW) method³⁶ as implemented in Vienna *Ab initio* Simulation Package (VASP).^{37–40} A basis set of plane waves with kinetic energy up to 600 eV was used to represent the Kohn-Sham orbitals, while the Brillouin zones were sampled by Monkhorst-Pack k -point meshes of no less than $7 \times 7 \times 7$. The van der Waals dispersion interactions, expected to describe the nonbonding interactions between the organic cations A and the inorganic framework BX_6 , were estimated with the nonlocal density functional vdW-DF2.⁴¹ Refitted Perdew-Wang 86,⁴² the GGA XC functional associated with vdW-DF2, was used for the geometry optimization, for which convergence was assumed when the atomistic forces become less than 0.01 eV/Å.

The electronic structures of solids, when being computed using GGA DFT, are known⁴³ to be systematically distorted, i.e., the conduction bands are rigidly shifted down and the bandgap is dramatically underestimated. This deficiency, if not fixed, will lead to serious errors in calculating the optical properties of the HOIPs. Therefore, we used two hybrid functionals, namely, HSE06^{28,29} and metaGGA (TB-MB),^{44,45} for the calculations of the properties related to electronic structures. More details on the calculations are given in Secs. III C and III D.

III. LEAD-FREE HOIPs FOR SOLAR CELL APPLICATIONS

Our refined HSE06 bandgap screening singles out 4 HOIPs, including methylammonium tin iodide $\text{CH}_3\text{NH}_3\text{SnI}_3$, formamidinium tin iodide $\text{HC}(\text{NH}_2)_2\text{SnI}_3$, hydrazinium tin iodide $\text{NH}_2\text{NH}_3\text{SnI}_3$, and azetidinium tin iodide $\text{NH}_2(\text{CH}_2)_3\text{SnI}_3$, which are summarized in Table I and visualized in Fig. 1. Of these four materials, $\text{CH}_3\text{NH}_3\text{SnI}_3$ and $\text{HC}(\text{NH}_2)_2\text{SnI}_3$ were synthesized experimentally in the pseudocubic phases^{23–25} and studied computationally.²² The agreement between the computed and measured lattice parameters of $\text{CH}_3\text{NH}_3\text{SnI}_3$ and $\text{HC}(\text{NH}_2)_2\text{SnI}_3$ is very good, confirming that the examined structures are those experimentally realized. All four HOIPs are based on SnI_3 , indicating that Sn is a potential alternative of Pb in lead-free solar cell HOIPs.

TABLE I. Summary of four pseudocubic lead-free hybrid organic-inorganic perovskite candidates for solar cell applications. The computed lattice parameter a^{comp} is obtained using GGA, while three values given for computed E_g are obtained using GGA, HSE06, and metaGGA functionals, respectively. Experimental values of the lattice parameter and bandgap are given with the corresponding references. a^{comp} is given in a range because the anisotropic cation A slightly distorts the ideal cubic geometry of the host perovskite structure. The electron and hole effective masses are given in unit of electron mass m_e .

Materials	a^{comp} (Å)	a^{exp} (Å)	$E_f(\frac{\text{eV}}{\text{atom}})$	E_g^{comp} (eV)			E_g^{exp} (eV)	m^* (m_e)	
				GGA	HSE06	metaGGA		Electron	Hole
$\text{CH}_3\text{NH}_3\text{SnI}_3$	6.48–6.60	$6.17^{23}, 6.23^{25}$	−0.39	1.17	1.65	1.57	$1.23\text{--}1.35^{23\text{--}25}$	0.49	0.32
$\text{HC}(\text{NH}_2)_2\text{SnI}_3$	6.53–6.61	6.33^{25}	−0.38	1.28	1.75	1.70	1.41^{25}	0.36	0.23
$\text{NH}_2\text{NH}_3\text{SnI}_3$	6.44–6.57	...	−0.32	1.18	1.63	1.47	...	0.22	0.17
$\text{NH}_2(\text{CH}_2)_3\text{SnI}_3$	6.59–6.80	...	−0.25	1.29	1.80	1.68	...	0.37	0.24

A. Stabilities

The formation (atomization) energy E_f of $\text{CH}_3\text{NH}_3\text{SnI}_3$, $\text{HC}(\text{NH}_2)_2\text{SnI}_3$, $\text{NH}_2\text{NH}_3\text{SnI}_3$, and $\text{NH}_2(\text{CH}_2)_3\text{SnI}_3$ was computed and is shown in Table I. The reference materials for evaluating E_f are the α -Sn (gray tin, space group $Fd3m$) phase of tin,⁴⁶ the orthorhombic $Cmca$ phase of iodine,⁴⁷ the graphite phase of carbon, and molecules N_2 and H_2 . The computed E_f ranges from −0.4 to −0.25 eV/atom, the typical value of stable solid materials that has been measured, computed, and reported in the literature.^{11,12,48–50} In fact, the cubic structural phases predicted for $\text{CH}_3\text{NH}_3\text{SnI}_3$ and $\text{HC}(\text{NH}_2)_2\text{SnI}_3$ were synthesized experimentally,^{23–25} thus, $\text{NH}_2\text{NH}_3\text{SnI}_3$ and $\text{NH}_2(\text{CH}_2)_3\text{SnI}_3$ are believed to be thermodynamically stable as well.

In computational studies, a solid material is typically considered to be dynamically stable if it does not have (unstable) imaginary phonon modes. This assessment is quite reliable for hard materials governed by strong interactions, e.g., those with covalent and/or ionic nature, in which vibration amplitudes are small. Similar to polymers, HOIPs contain not only such strong interactions but also very weak dispersion interactions. In these materials, the vibrational spectrum could range from ≤ 1 THz for the rotational vibrations of the cation A and the BX_6 octahedral tilting to over ≥ 100 THz with the stretching modes of the C–H and N–H bonds.⁵¹ Because the low-frequency regime of this spectrum is comparable with the level of

numerical noise,^{22,34} calculating phonon structures of HOIPs using DFT is usually very challenging.^{22,52}

Herein, we used PHONOPY,^{53,54} which implements the supercell approach, to compute the phonon band structure of $\text{CH}_3\text{NH}_3\text{SnI}_3$, $\text{HC}(\text{NH}_2)_2\text{SnI}_3$, $\text{NH}_2\text{NH}_3\text{SnI}_3$, and $\text{NH}_2(\text{CH}_2)_3\text{SnI}_3$. The computed phonon band structures, shown in the supplementary material, contain essentially no dynamically unstable modes. A soft mode with an imaginary frequency of ~ -0.4 THz is found at point $N(-0.5, -0.5, 0.5)$ of $\text{NH}_2\text{NH}_3\text{SnI}_3$, which was found to correspond to the BX_6 octahedral tilting and the rotations of the NH_2NH_3 cation, as reported for other HOIPs.^{22,52} Overall, all the predicted structures of $\text{CH}_3\text{NH}_3\text{SnI}_3$, $\text{HC}(\text{NH}_2)_2\text{SnI}_3$, $\text{NH}_2\text{NH}_3\text{SnI}_3$, and $\text{NH}_2(\text{CH}_2)_3\text{SnI}_3$ are dynamically stable.

B. Electronic structures and properties

The electronic structures of the four selected HOIPs, computed at the metaGGA level of DFT, are given in Fig. 2. All of them are direct-bandgap materials with both valence-band maximum (VBM) and conduction-band minimum (CBM) locating at N . The density of electronic states, given in the supplementary material, indicates that the CBM of these HOIPs is mainly contributed by Sn $5p$ states, and their VBM is dominated by contributions from I $5p$ states, being consistent with a previous report for $\text{CH}_3\text{NH}_3\text{SnI}_3$.^{55,56} Therefore,

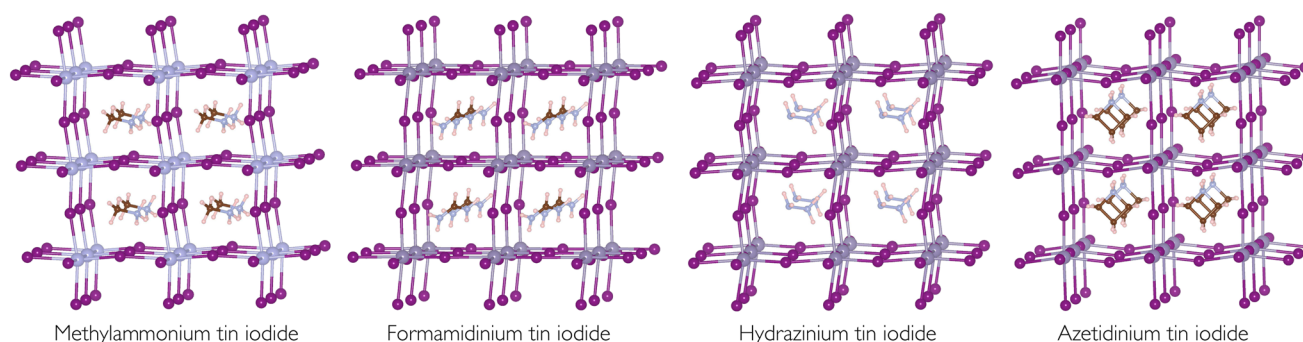


FIG. 1. Four computationally identified lead-free hybrid organic-inorganic perovskites, in which the first two have been realized,^{23–25} while the others remain hypothetical. The organic cations of these HOIPs are, from left to right, methylammonium CH_3NH_3 , formamidinium $\text{HC}(\text{NH}_2)_2$, hydrazinium NH_2NH_3 , and azetidinium $\text{NH}_2(\text{CH}_2)_3$.

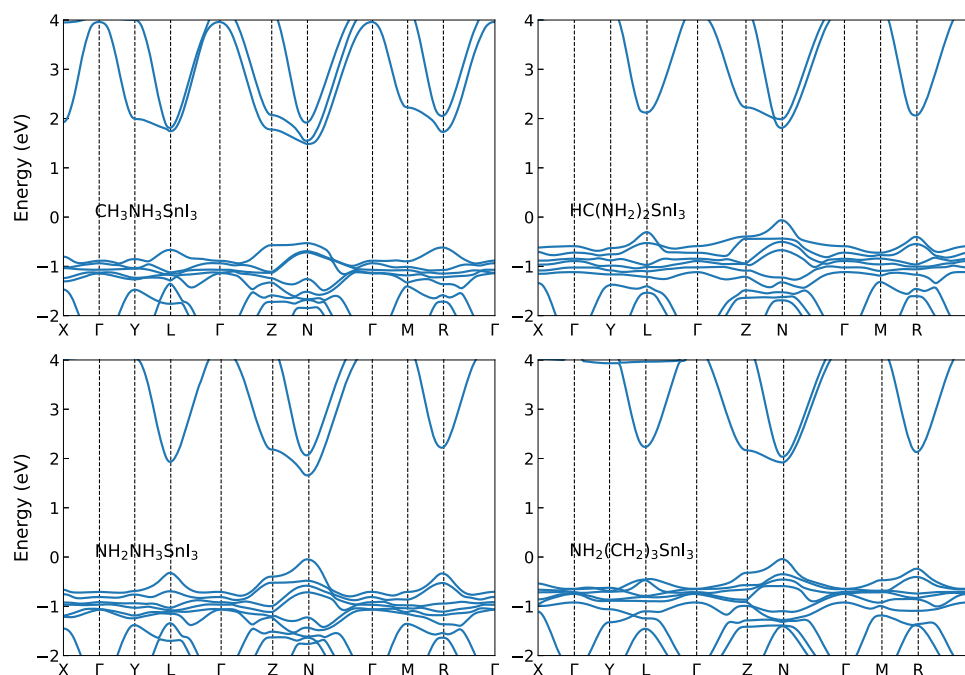


FIG. 2. Electronic structures of methylammonium tin iodide $\text{CH}_3\text{NH}_3\text{SnI}_3$, formamidinium tin iodide $\text{HC}(\text{NH}_2)_2\text{SnI}_3$, hydrazinium tin iodide $\text{NH}_2\text{NH}_3\text{SnI}_3$, and azetidinium tin iodide $\text{NH}_2(\text{CH}_2)_3\text{SnI}_3$, computed at the GGA level of DFT, incorporating the vdW-DF2 functional for the vdW interactions.

once created by photon absorption, electron-hole pairs are spatially separated, and this could lead to longer carrier lifetime.

The bandgap of these HOIPs, computed at the GGA, HSE06, and metaGGA levels of DFT, is given in Table I. Compared to the experimentally measured bandgap of $\text{CH}_3\text{NH}_3\text{SnI}_3$ and $\text{HC}(\text{NH}_2)_2\text{SnI}_3$, the GGA values are slightly smaller, while the HSE06 and metaGGA hybrid XC functionals slightly overestimate E_g . The bandgap of all four materials falls within the lower part of the visible light spectrum, being optimal for the power conversion efficiency, according to Shockley and Queisser.⁵⁷ In addition, the carrier effective mass was extracted directly from the electronic band structures and is reported in Table I. For all of the HOIPs, the effective mass is small, ranging from about $0.15m_e$ to $0.5m_e$, being comparable with the carrier effective mass recently computed for tetragonal $\text{CH}_3\text{NH}_3\text{SnI}_3$.⁵⁶ Such small carriers are desirable for a solar cell absorber, which collect a fairly small amount of energy carried by the incident photons.

C. Optical properties

We used the numerical scheme⁵⁸ developed within the PAW methodology and implemented in VASP for computing the frequency-dependent dielectric function $\epsilon(\omega) = \epsilon^{(1)}(\omega) + i\epsilon^{(2)}(\omega)$ of the HOIPs at the long-wavelength limit. Within this scheme, the imaginary part of the dielectric tensor is computed by a summation over the possible optical transitions which are closely connected to the electronic spectrum $\{\epsilon_k\}$ is⁵⁸

$$\epsilon_{\alpha\beta}^{(2)}(\omega) = \frac{4\pi^2 e^2}{\Omega} \lim_{q \rightarrow 0} \frac{1}{q^2} \sum_{c,v,\mathbf{k}} 2w_{\mathbf{k}} \delta(\epsilon_{c\mathbf{k}} - \epsilon_{v\mathbf{k}} - \omega) \times \langle u_{c\mathbf{k}+\hat{\mathbf{e}}_{\alpha}q} | u_{v\mathbf{k}} \rangle \langle u_{c\mathbf{k}+\hat{\mathbf{e}}_{\beta}q} | u_{v\mathbf{k}}^* \rangle, \quad (1)$$

where c and v are indices of the conduction and valence bands, respectively, $\hat{\mathbf{e}}_{\alpha/\beta}$ is the unit vector along the α/β Cartesian directions, $w_{\mathbf{k}}$ is the weight factor of \mathbf{k} in the sampled first Brillouin zone, Ω is the volume of the primitive cell, and $u_{c\mathbf{k}}$ is the (periodic function) magnitude of $e^{i\mathbf{k}\cdot\mathbf{r}}$ in Bloch's theorem. The real part of the dielectric tensor follows from the Kramers-Kronig transformation

$$\epsilon_{\alpha\beta}^{(1)}(\omega) = 1 + \frac{2}{\pi} \mathcal{P} \int_0^\infty d\omega' \frac{\epsilon_{\alpha\beta}^{(2)}(\omega') \omega'}{\omega'^2 - \omega^2}, \quad (2)$$

where \mathcal{P} denotes the principal values. Then, the macroscopic dielectric function is given by $\epsilon(\omega) = \sum_{\alpha\beta} \hat{\mathbf{e}}_{\alpha} \epsilon_{\alpha\beta}(\omega) \hat{\mathbf{e}}_{\beta}$, from which important optical-related properties, such as the absorption coefficient $I(\omega)$, are computed,

$$I(\omega) = \sqrt{2\omega} \left[\sqrt{\epsilon^{(1)}(\omega)^2 + \epsilon^{(2)}(\omega)^2} - \epsilon^{(1)}(\omega) \right]^{1/2}. \quad (3)$$

The primary challenge of using DFT for this scheme is essentially technical in nature. In particular, the unoccupied Kohn-Sham eigenvalues $\{\epsilon_{c\mathbf{k}}\}$ are significantly lowered at the GGA level of DFT,⁴³ while computing a sufficiently large number of $\{\epsilon_{c\mathbf{k}}\}$ using the HSE06 XC functional at all the \mathbf{k} points needed to sample the Brillouin zone, according to Eq. (1), is computationally prohibitive. Here, we used the metaGGA functional for better computing $\{\epsilon_{c\mathbf{k}}\}$, although this work remains very expensive. The validity of this numerical approach is demonstrated in Sec. III D within a discussion of the results shown in Table II.

The electronic band structure of $\text{NH}_2\text{NH}_3\text{SnI}_3$ computed using the GGA and metaGGA XC correlation functions is shown in Fig. 3. While the valence bands are essentially changed, the conduction bands are rigidly shifted up when the metaGGA functional is used.

TABLE II. Short-circuit current density J_{sc} , given in mA/cm^2 , and SLME η , given in %, computed for the examined HOIPs. The results reported herein were estimated at the absorber layer thickness of $L = 2000$ nm, when J_{sc} and η saturate (see Fig. 4 for more information). Experimental data of J_{sc} and PCE are also given.

Materials	J_{sc}^{comp}	J_{sc}^{expt}	η^{comp}	PCE^{expt}
$\text{CH}_3\text{NH}_3\text{SnI}_3$	24.0	11.8–21.4 ¹⁷	31.0	1.7–6.4 ¹⁷
$\text{HC}(\text{NH}_2)_2\text{SnI}_3$	23.0	17.17–24.5 ¹⁷	28.2	2.1–6.6 ¹⁷
$\text{NH}_2\text{NH}_3\text{SnI}_3$	24.6	...	32.0	...
$\text{NH}_2(\text{CH}_2)_3\text{SnI}_3$	21.2	...	28.4	...

Three groups of direct optical transitions can be found near the N, L, and R points with $\omega \approx 1.7$ eV, 2.1 eV, and 2.4 eV. These transitions are translated to three significant peaks in the computed dielectric functions $\epsilon(\omega)$ and the absorption coefficient $I(\omega)$ of $\text{NH}_2\text{NH}_3\text{SnI}_3$, also given in Fig. 3. Among four HOIPs considered, $\text{CH}_3\text{NH}_3\text{SnI}_3$ exhibits considerably higher dielectric functions $\epsilon(\omega)$ and absorption coefficient $I(\omega)$, probably because of the nearly multiple degenerate unoccupied bands at N, L, and R points.

D. Spectroscopic limited maximum efficiency

The power conversion efficiency (PCE) of a solar absorber is also a very important parameter, but estimating such a quantity is nontrivial. In particular, the very high PCE of $\text{CH}_3\text{NH}_3\text{SnI}_3$ was attributed to the excellent carrier transport properties,^{59,60} for which calculations at an acceptable level of fidelity are either

impossible or exceedingly computationally demanding.⁶¹ Therefore, simple phenomenological measures of PCE are quite useful for quick screening purposes. One of such measures was introduced by Shockley and Queisser,⁵⁷ using the bandgap of the material being considered and the blackbody radiation and the solar spectrum information. More recently, spectroscopic limited maximum efficiency (SLME) was introduced,⁶² adding the absorptivity, which encodes information on the dipole matrix elements and absorber layer thickness, into consideration. However, it is noted here that SLME is essentially a *qualitative* measure, somehow giving the upper bound of PCE. Because computing SLME is not intensive nor complicated when the optical properties (as those discussed in Sec. III C) are available, this concept was used^{65–69} quite frequently for quickly identifying promising candidates for a solar absorber.

In summary, the spectroscopic limited maximum efficiency η is defined and thus computed as

$$\eta \equiv \frac{P_{\text{max}}}{P_{\text{in}}} = \frac{\max\left\{J_{sc} - J_0\left(e^{eV/k_B T} - 1\right)\right\}_V}{\int_0^\infty EI_{\text{sun}}(E)dE}, \quad (4)$$

where V is the potential over the absorber layer and k_B is the Boltzmann constant. Two important parameters for computing η using Eq. (4), namely, the short-circuit current density J_{sc} and the reverse saturation current density J_0 , were estimated from the AM1.5G solar spectrum $I_{\text{sun}}(\omega)$ and the black-body spectrum $I_{\text{bb}}(\omega, T)$ as

$$J_{sc} = e \int_0^\infty a(\omega) I_{\text{sun}}(\omega) d\omega \quad (5)$$

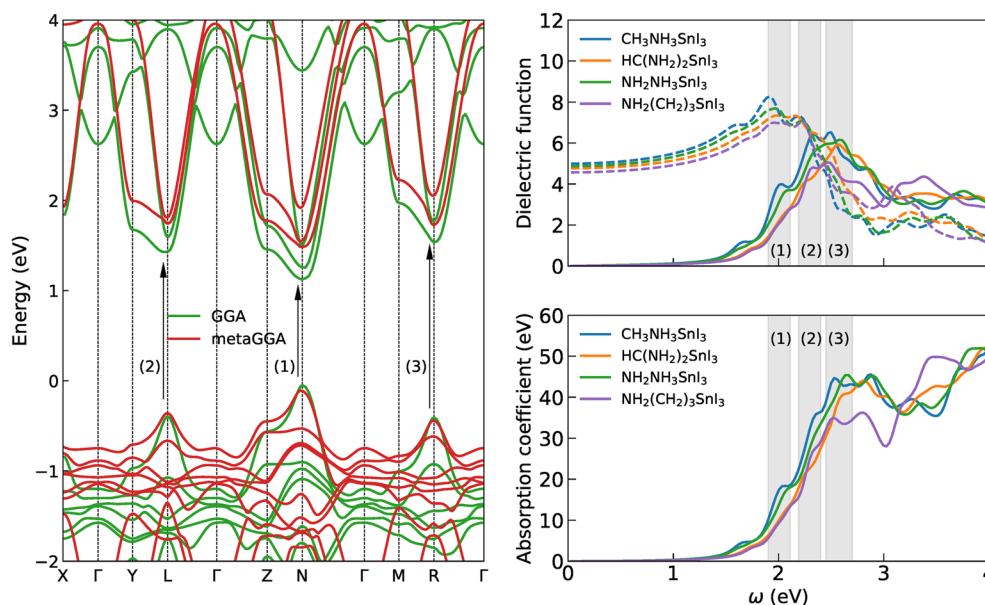


FIG. 3. Left: electronic structure of $\text{NH}_2\text{NH}_3\text{SnI}_3$ computed at the GGA and metaGGA levels of DFT in which three arrows indicate the first three groups of optical transitions (1), (2), and (3); top right: the dielectric function $\epsilon(\omega)$ and bottom right: the absorption coefficient $I(\omega)$ of methylammonium tin iodide $\text{CH}_3\text{NH}_3\text{SnI}_3$, formamidinium tin iodide $\text{HC}(\text{NH}_2)_2\text{SnI}_3$, hydrazinium tin iodide $\text{NH}_2\text{NH}_3\text{SnI}_3$, and azetidinium tin iodide $\text{NH}_2(\text{CH}_2)_3\text{SnI}_3$. In the top right panel, solid and dashed lines are used for the imaginary and real dielectric functions, i.e., $\epsilon^{(2)}(\omega)$ and $\epsilon^{(1)}(\omega)$, respectively. Three shaded regions indicate three peaks of $\epsilon^{(2)}(\omega)$ and $I(\omega)$ that correspond to three groups of transitions shown in the left panel.

and

$$J_0 \equiv \frac{J_0^r}{f_r} = \frac{e\pi}{f_r} \int_0^\infty a(\omega) I_{bb}(\omega, T) d\omega. \quad (6)$$

Here, the absorptivity $a(\omega) = 1 - e^{-2I(\omega)L/(2\pi\hbar c)}$ with \hbar being the Planck constant, c being the speed of light, and L being the absorber layer thickness. The fraction of radiative recombination f_r is given by $f_r = e^{[(E_g^{\text{da}} - E_g)/(k_B T)]}$, where E_g^{da} is the direct allowed bandgap over which direct optical transitions may occur, as shown in Fig. 3. For direct bandgap materials, $E_g^{\text{da}} = E_g$, and thus, $f_r = 1$.

The computed short-circuit current density J_{sc} of 4 examined HOIPs is given in Table II. Compared to the available experimental data, our computed results are very well consistent. Given that J_{sc} was computed from $a(\omega)$ using Eq. (5), this agreement strongly indicates that the numerical scheme, described in Sec. III C and used to calculate the absorptivity $a(\omega)$ and the absorption coefficient $I(\omega)$, is essentially reasonable.

The spectroscopic limited maximum efficiency η (as a function of the absorber layer thickness L) computed for the four HOIPs considered in this work is given in Fig. 4. For all the materials, η saturates at about 1000 nm and higher, being consistent with all the calculations in the literature.^{64–67} Although the absorption coefficient $I(\omega)$ of $\text{NH}_3\text{NH}_2\text{SnI}_3$ is lower than that of $\text{CH}_3\text{NH}_3\text{SnI}_3$, the former is slightly higher than the latter in SLME ($\eta \approx 30\%–32\%$) probably because its fundamental bandgap is closer to the optimal range bandgaps for solar absorbers (≈ 1.4 eV).⁵⁷ This result indicates that, in terms of SLME, $\text{CH}_3\text{NH}_3\text{SnI}_3$, $\text{HC}(\text{NH}_2)_2\text{SnI}_3$, $\text{NH}_3\text{NH}_2\text{SnI}_3$, and $\text{NH}_2(\text{CH}_2)_3\text{SnI}_3$ are comparable to the best candidates among thousands of most promising solar absorbers recently studied in Refs. 64–67, specifically Ga-doped $\text{CH}_3\text{NH}_3\text{PbI}_3$.⁶⁸

However, compared to the experimental PCE of $\text{CH}_3\text{NH}_3\text{SnI}_3$ and $\text{HC}(\text{NH}_2)_2\text{SnI}_3$, the computed SLME is significantly overestimated by a factor of about 5–15. Although SLME was widely used in the past^{63–67} as an upper limit of PCE, we believe that Eq. (4) is an

inadequate model. One of the possible reasons for the large disagreement is that morphology-related factors of the materials have not been considered. To be more specific, the current numerical scheme (and all the practical calculations) assumes infinite crystalline materials, while the interfaces of the fabricated devices were not modeled, and the absorber layer may contain a good amount of amorphous materials that dramatically alter the materials' electronic structure and optical properties. Clearly, an improved model for SLME is desirable.

IV. IMPLICATIONS AND PERSPECTIVES

Materials data play the role of fuel for running the rapidly developing field of materials informatics.² Major materials databases such as Materials Project,³ Open Quantum Materials Databases,⁶ and NoMAD host hundreds of thousands of organic materials. However, for polymers⁹ and organic-inorganic hybrid materials,^{10,21} computational data remain small mostly because preparing reasonable atomic structures is very challenging. Due to the enormous computational resource needed for the HOIP structure predictions at the first-principles level, the dataset used for this work only contains the pseudocubic-like phases, i.e., those having one formula unit per primitive cell. The realization of some pseudocubic HOIPs^{23–25} of this dataset implies its certain suitability. However, we also believe that a bigger and better dataset of HOIPs is now a pressing need, and once available, it will become much more useful for the community.

Despite the rising role of data-driven approaches, they should be complemented by physics-based computational methods such as DFT and beyond. We have shown that, at the current status, the latest version of such methods is reasonable for computing the electronic structure and optical properties of the HOIPs. On the contrary, further developments on predicting the power conversion efficiency are needed as current methods for this very important property of solar cell materials remain rather off. Large-scale simulation methods are also needed as a reasonable model for describing morphology-scale characteristics of the materials far beyond the reach of DFT-based methods. Along this line, machine-learning force fields^{69,70} may be a feasible approach.

V. SUMMARY AND CONCLUSIONS

Starting from a recently developed dataset of 1346 HOIPs, we have identified four lead-free materials, including $\text{CH}_3\text{NH}_3\text{SnI}_3$, $\text{HC}(\text{NH}_2)_2\text{SnI}_3$, $\text{NH}_3\text{NH}_2\text{SnI}_3$, and $\text{NH}_2(\text{CH}_2)_3\text{SnI}_3$, to be promising candidates for photovoltaic applications. Our first-principles computations using DFT show that they have preferable electronic structures and carrier effective mass, good optical properties, and very high spectroscopic limited maximum efficiency η . Compared to the recent experimental data of $\text{CH}_3\text{NH}_3\text{SnI}_3$ and $\text{HC}(\text{NH}_2)_2\text{SnI}_3$, we found that our computational results for electronic and optical properties are in good agreement, while the approach of spectroscopic limited maximum efficiency η should be further improved to better reach the power conversion efficiency. Based on the computational prediction, we suggest that $\text{NH}_3\text{NH}_2\text{SnI}_3$ and $\text{NH}_2(\text{CH}_2)_3\text{SnI}_3$ are worth testing experimentally. We also highlight the impact of the recent data development in materials informatics and suggest that big and diverse data in this

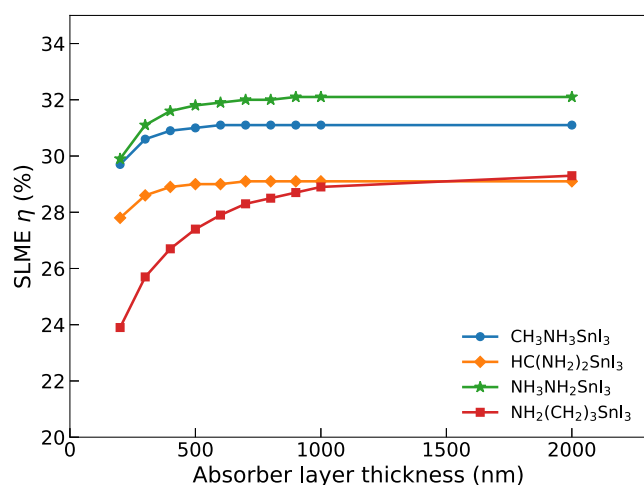


FIG. 4. The spectroscopic limited maximum efficiency η computed for the four HOIPs using the metaGGA electronic structure.

emerging field will be very useful for the community. In the specific case of HOIPs, the HOIP dataset¹⁰ is significantly diverse in terms of chemistry and structural motifs, containing some materials at any range of bandgaps of interest. We suggest that it should further be expanded, accumulating additional organic cations A and considering larger models.

SUPPLEMENTARY MATERIAL

The [supplementary material](#) is available for this paper, providing the atomic structure of $\text{CH}_3\text{NH}_3\text{SnI}_3$, $\text{HC}(\text{NH}_2)_2\text{SnI}_3$, $\text{NH}_3\text{NH}_2\text{SnI}_3$, and $\text{NH}_2(\text{CH}_2)_3\text{SnI}_3$, the computed phonon band structures of these 4 HOIPs, and the computed (projected) electronic density of states of $\text{NH}_3\text{NH}_2\text{SnI}_3$.

ACKNOWLEDGMENTS

Research is supported by Vingroup Innovation Foundation (VINIF) in project code VINIF.2019.DA03. The authors thank Marnik Berx (University of Antwerp) for useful discussions and acknowledge computational support from XSEDE under Grant No. TG-DMR170031. The structures of the HOIPs reported in this work are available in the [supplementary material](#) and at <http://godeepdata.org/>.

REFERENCES

- ¹K. Rajan, *Mater. Today* **8**, 38 (2005).
- ²R. Ramprasad, R. Batra, G. Pilania, A. Mannodi-Kanakkithodi, and C. Kim, *npj Comput. Mater.* **3**, 54 (2017).
- ³C. Kim, A. Chandrasekaran, T. D. Huan, D. Das, and R. Ramprasad, *J. Phys. Chem. C* **122**, 17575 (2018).
- ⁴T. D. Huan, A. Mannodi-Kanakkithodi, and R. Ramprasad, *Phys. Rev. B* **92**, 014106 (2015).
- ⁵A. Jain, S. P. Ong, G. Hautier, W. Chen, W. D. Richards, S. Dacek, S. Cholia, D. Gunter, D. Skinner, G. Ceder, and K. A. Persson, *APL Mater.* **1**, 011002 (2013).
- ⁶J. E. Saal, S. Kirklin, M. Aykol, B. Meredig, and C. Wolverton, *JOM* **65**, 1501 (2013).
- ⁷P. Hohenberg and W. Kohn, *Phys. Rev.* **136**, B864 (1964).
- ⁸W. Kohn and L. Sham, *Phys. Rev.* **140**, A1133 (1965).
- ⁹T. D. Huan, A. Mannodi-Kanakkithodi, C. Kim, V. Sharma, G. Pilania, and R. Ramprasad, *Sci. Data* **3**, 160012 (2016).
- ¹⁰C. Kim, T. D. Huan, S. Krishnan, and R. Ramprasad, *Sci. Data* **4**, 170057 (2017).
- ¹¹T. D. Huan, *Phys. Rev. Mater.* **2**, 023803 (2018).
- ¹²V. N. Tuoc and T. D. Huan, *J. Phys. Chem. C* **122**, 17067 (2018).
- ¹³Organic-Inorganic Halide Perovskite Photovoltaics: From Fundamentals to Device Architectures, edited by M. Grätzel, T. Miyasaka, and N.-G. Park (Springer International Publishing, Switzerland, 2016).
- ¹⁴A. K. Jena, A. Kulkarni, and T. Miyasaka, *Chem. Rev.* **119**, 3036 (2019).
- ¹⁵C. C. Boyd, R. Cheacharoen, T. Leijtens, and M. D. McGehee, *Chem. Rev.* **119**, 3418 (2019).
- ¹⁶F. Giustino and H. J. Snaith, *ACS Energy Lett.* **1**, 1233 (2016).
- ¹⁷L. Liang and P. Gao, *Adv. Sci.* **5**, 1700331 (2018).
- ¹⁸D. P. McMeekin, G. Sadoughi, W. Rehman, G. E. Eperon, M. Saliba, M. T. Hörantner, A. Haghighirad, N. Sakai, L. Korte, B. Rech, M. B. Johnston, L. M. Herz, and H. J. Snaith, *Science* **351**, 151 (2016).
- ¹⁹Z. Li, M. Yang, J.-S. Park, S.-H. Wei, J. J. Berry, and K. Zhu, *Chem. Mater.* **28**, 284 (2016).
- ²⁰Z. Wang, Q. Lin, B. Wenger, M. G. Christoforo, Y.-H. Lin, M. T. Klug, M. B. Johnston, L. M. Herz, and H. J. Snaith, *Nat. Energy* **3**, 855 (2018).
- ²¹I. E. Castelli, J. M. García-Lastra, K. S. Thygesen, and K. W. Jacobsen, *APL Mater.* **2**, 081514 (2014).
- ²²T. D. Huan, V. N. Tuoc, and N. V. Minh, *Phys. Rev. B* **93**, 094105 (2016).
- ²³F. Hao, C. C. Stoumpos, D. H. Cao, R. P. H. Chang, and M. G. Kanatzidis, *Nat. Photonics* **8**, 489 (2014).
- ²⁴Y. Yu, D. Zhao, C. R. Grice, W. Meng, C. Wang, W. Liao, A. J. Cimaroli, H. Zhang, K. Zhu, and Y. Yan, *RSC Adv.* **6**, 90248 (2016).
- ²⁵C. C. Stoumpos, C. D. Malliakas, and M. G. Kanatzidis, *Inorg. Chem.* **52**, 9019 (2013).
- ²⁶D. C. Langreth and M. J. Mehl, *Phys. Rev. B* **28**, 1809 (1983).
- ²⁷A. D. Becke, *Phys. Rev. A* **38**, 3098 (1988).
- ²⁸J. Heyd, G. E. Scuseria, and M. Ernzerhof, *J. Chem. Phys.* **118**, 8207 (2003).
- ²⁹J. Heyd, G. E. Scuseria, and M. Ernzerhof, *J. Chem. Phys.* **124**, 219906 (2006).
- ³⁰S. Goedecker, *J. Chem. Phys.* **120**, 9911 (2004).
- ³¹M. Amsler and S. Goedecker, *J. Chem. Phys.* **133**, 224104 (2010).
- ³²T. D. Huan, M. Amsler, V. N. Tuoc, A. Willand, and S. Goedecker, *Phys. Rev. B* **86**, 224110 (2012).
- ³³T. D. Huan, M. Amsler, R. Sabatini, V. N. Tuoc, N. B. Le, L. M. Woods, N. Marzari, and S. Goedecker, *Phys. Rev. B* **88**, 024108 (2013).
- ³⁴H. D. Tran, M. Amsler, S. Botti, M. A. L. Marques, and S. Goedecker, *J. Chem. Phys.* **140**, 124708 (2014).
- ³⁵T. D. Huan, V. N. Tuoc, N. B. Le, N. V. Minh, and L. M. Woods, *Phys. Rev. B* **93**, 094109 (2016).
- ³⁶P. E. Blöchl, *Phys. Rev. B* **50**, 17953 (1994).
- ³⁷G. Kresse and J. Hafner, *Phys. Rev. B* **47**, 558 (1993).
- ³⁸G. Kresse, “*Ab initio* molekular dynamik für flüssige metalle,” Ph.D. thesis, Technische Universität Wien, 1993.
- ³⁹G. Kresse and J. Furthmüller, *Comput. Mater. Sci.* **6**, 15 (1996).
- ⁴⁰G. Kresse and J. Furthmüller, *Phys. Rev. B* **54**, 11169 (1996).
- ⁴¹K. Lee, É. D. Murray, L. Kong, B. I. Lundqvist, and D. C. Langreth, *Phys. Rev. B* **82**, 081101(R) (2010).
- ⁴²E. D. Murray, K. Lee, and D. C. Langreth, *J. Chem. Theory Comput.* **5**, 2754 (2009).
- ⁴³J. P. Perdew, *Int. J. Quantum Chem.* **28**, 497 (1985).
- ⁴⁴F. Tran and P. Blaha, *Phys. Rev. Lett.* **102**, 226401 (2009).
- ⁴⁵A. D. Becke and E. R. Johnson, *J. Chem. Phys.* **124**, 221101 (2006).
- ⁴⁶L. Brownlee, *Nature* **166**, 482 (1950).
- ⁴⁷P. M. Harris, E. Mack, Jr., and F. Blake, *J. Am. Chem. Soc.* **50**, 1583 (1928).
- ⁴⁸W. M. Haynes, *CRC Handbook of Chemistry and Physics* (CRC Press, USA, 2012).
- ⁴⁹R. Sharma and Y. Chang, *Bull. Alloy Phase Diagrams* **7**, 269 (1986).
- ⁵⁰A. Novoselova, V. Zlomanov, S. Karbanov, O. Matveyev, and A. Gas'kov, *Prog. Solid State Chem.* **7**, 85 (1972).
- ⁵¹I. P. Swainson, C. Stock, S. F. Parker, L. Van Eijck, M. Russina, and J. W. Taylor, *Phys. Rev. B* **92**, 100303 (2015).
- ⁵²F. Brivio, J. M. Frost, J. M. Skelton, A. J. Jackson, O. J. Weber, M. T. Weller, A. R. Goñi, A. M. A. Leguy, P. R. F. Barnes, and A. Walsh, *Phys. Rev. B* **92**, 144308 (2015).
- ⁵³A. Togo, F. Oba, and I. Tanaka, *Phys. Rev. B* **78**, 134106 (2008).
- ⁵⁴K. Parlinski, Z. Q. Li, and Y. Kawazoe, *Phys. Rev. Lett.* **78**, 4063 (1997).
- ⁵⁵P.-P. Sun, Q.-S. Li, L.-N. Yang, and Z.-S. Li, *Nanoscale* **8**, 1503 (2016).
- ⁵⁶P. Umari, E. Mosconi, and F. D. Angelis, *Sci. Rep.* **4**, 4467 (2014).
- ⁵⁷W. Shockley and H. J. Queisser, *J. Appl. Phys.* **32**, 510 (1961).
- ⁵⁸M. Gajdoš, K. Hummer, G. Kresse, J. Furthmüller, and F. Bechstedt, *Phys. Rev. B* **73**, 045112 (2006).
- ⁵⁹D. W. de Quilettes, S. M. Vorpahl, S. D. Stranks, H. Nagaoka, G. E. Eperon, M. E. Ziffer, H. J. Snaith, and D. S. Ginger, *Science* **348**, 683 (2015).
- ⁶⁰S. D. Stranks and H. J. Snaith, *Nat. Nanotechnol.* **10**, 391 (2015).
- ⁶¹T. Hakamata, K. Shimamura, F. Shimajo, R. K. Kalia, A. Nakano, and P. Vashishta, *Sci. Rep.* **6**, 19599 (2016).
- ⁶²L. Yu and A. Zunger, *Phys. Rev. Lett.* **108**, 068701 (2012).
- ⁶³L. Yu, R. S. Kokenyesi, D. A. Keszler, and A. Zunger, *Adv. Energy Mater.* **3**, 43 (2013).

- ⁶⁴M. Bercx, N. Sarmadian, R. Saniz, B. Partoens, and D. Lamoen, [Phys. Chem. Chem. Phys.](#) **18**, 20542 (2016).
- ⁶⁵N. Sarmadian, R. Saniz, B. Partoens, and D. Lamoen, [J. Appl. Phys.](#) **120**, 085707 (2016).
- ⁶⁶J. Wang, H. Chen, S.-H. Wei, and W.-J. Yin, [Adv. Mater.](#) **31**, 1806593 (2019).
- ⁶⁷D. H. Fabini, M. Koerner, and R. Seshadri, [Chem. Mater.](#) **31**, 1561 (2019).
- ⁶⁸R. Mayengbam, A. Srivastava, S. K. Tripathy, and G. Palai, [J. Phys. Chem. C](#) **123**, 23323 (2019).
- ⁶⁹T. D. Huan, R. Batra, J. Chapman, C. Kim, A. Chandrasekaran, and R. Ramprasad, [J. Phys. Chem. C](#) **123**, 20715 (2019).
- ⁷⁰R. Jinnouchi, J. Lahnsteiner, F. Karsai, G. Kresse, and M. Bokdam, [Phys. Rev. Lett.](#) **122**, 225701 (2019).